Nanoparticles Targeted to Fibroblast Activation Protein Outperform PSMA for MRI Delineation of Primary Prostate Tumors

Nicole Dmochowska, Valentina Milanova, Ramesh Mukkamala, Kwok Keung Chow, Nguyen T. H. Pham, Madduri Srinivasarao, Lisa M. Ebert, Timothy Stait-Gardner, Hien Le, Anil Shetty, Melanie Nelson, Philip S. Low, and Benjamin Thierry*

Accurate delineation of gross tumor volumes remains a barrier to radiotherapy dose escalation and boost dosing in the treatment of solid tumors, such as prostate cancer. Magnetic resonance imaging (MRI) of tumor targets has the power to enable focal dose boosting, particularly when combined with technological advances such as MRI-linear accelerator. Fibroblast activation protein (FAP) is overexpressed in stromal components of >90% of epithelial carcinomas. Herein, the authors compare targeted MRI of prostate specific membrane antigen (PSMA) with FAP in the delineation of orthotopic prostate tumors. Control, FAP, and PSMA-targeting iron oxide nanoparticles were prepared with modification of a lymphotropic MRI agent (FerroTrace, Ferronova). Mice with orthotopic LNCaP tumors underwent MRI 24 h after intravenous injection of nanoparticles. FAP and PSMA nanoparticles produced contrast enhancement on MRI when compared to control nanoparticles. FAP-targeted MRI increased the proportion of tumor contrast-enhancing black pixels by 13%, compared to PSMA. Analysis of changes in R2 values between healthy prostates and LNCaP tumors indicated an increase in contrast-enhancing pixels in the tumor border of 15% when targeting FAP, compared to PSMA. This study demonstrates the preclinical feasibility of PSMA and FAP-targeted MRI which can enable targeted image-guided focal therapy of localized prostate cancer.

1. Introduction

Prostate cancer (PCa) is one of the most diagnosed malignancies in men[1] and, owing to its relatively high survival rate and frequent full gland treatment-associated morbidity is the leading cause of treatment-related years lived with disability worldwide. Along with radical prostatectomy, radiotherapy is a mainstay treatment option for all stages of the disease and is commonly delivered as a uniform dose over the entire prostate gland.[2] There is mounting evidence that the risk of biochemical disease recurrence is reduced with dose escalation when using greater than 80 Gy, especially in patients with intermediate or high-risk lesions. However, dose intensification of the whole gland is limited by off-target toxicities to adjacent organs at risk including the rectum, urethra, and bladder.[3] Following pelvic radiotherapy, up to 30% of patients experience late grade III or IV

N. Dmochowska, V. Milanova, K. K. Chow, B. Thierry
Future Industries Institute
University of South Australia
Adelaide, South Australia 5095, Australia
E-mail: benjamin.thierry@unisa.edu.au

R. Mukkamala, M. Srinivasarao, P. S. Low
Department of Chemistry and Institute for Drug Discovery
Purdue University
West Lafayette, IN 47907, USA

N. T. H. Pham
Key Centre for Polymers and Colloids
School of Chemistry
The University of Sydney
Sydney, New South Wales 2006, Australia

L. M. Ebert
Centre for Cancer Biology
University of South Australia; SA Pathology; Cancer Clinical Trials Unit
Royal Adelaide Hospital; Adelaide Medical School
University of Adelaide
Adelaide, South Australia 5000, Australia

T. Stait-Gardner
Nanoscale Organisation and Dynamics Group
Western Sydney University
Sydney, New South Wales 2560, Australia

H. Le
Department of Radiation Oncology
Royal Adelaide Hospital
Adelaide, South Australia 5000, Australia

A. Shetty, M. Nelson
Ferronova Pty Ltd
Mawson Lakes, South Australia 5095, Australia

genitourinary or gastrointestinal toxicities, with persistent long-term negative impacts on quality of life, through both mental and physical wellbeing, largely due to bowel disturbances.[4,5] Although modern radiotherapy techniques enable safer and more precise dose delivery to the prostate, treatment-associated morbidity remains a significant concern in the treatment of PCa patients.

PCa is a multifocal disease, often presenting with large primary intraprostatic lesions accompanied by smaller, well-defined secondary lesions. Dominant intraprostatic lesions (index lesions) are considered to be the most aggressive, responsible for driving disease progression and prognosis, and are the most common sites of recurrence.[6–8] Focal dose escalation radiotherapy approaches specifically target index lesions, balancing the risk of recurrence and the patient's quality of life. For example, the recently reported FLAME study demonstrated that focal dose escalation under the guidance of multiparametric MRI (mpMRI) could improve biochemical recurrence-free survival by 7%, without impacting morbidity and quality of life.[9] Early results from a phase II trial investigating MRI-guided focused ultrasound ablation for localized intermediate-risk PCa also demonstrated encouraging oncologic and functional outcomes with 93% of patients disease-free at 5 months after treatment.[10] In a cohort of low to intermediate-risk PCa, gadolinium-enhanced MRI-guided focal laser ablation showed promising early oncologic results with 17% of participants requiring additional oncologic treatment after one year of initial treatment, with no significant side effects or impact on quality of life.[11]

Target delineation, a key requirement to define gross tumor volumes (GTV) in intraprostatic focal treatment approaches, is commonly referred to as the Achilles' heel of radiotherapy. Owing to its superior soft-tissue resolution compared to computed tomography and the ability to acquire non-invasive functional imaging, mpMRI is rapidly becoming a staple tool in guiding PCa radiotherapy and more generally focal ablation. Adoption is supported by powerful technological advances such as the integration of MRI with linear accelerators (MRI-LINAC) and MRI-ultrasound (US) fusion set-ups that streamline intraoperative US image guidance with the resolution of MRI. However, mpMRI only has a moderate inter-rater agreement and is prone to a large false-positive rate and underestimation of tumor margins.[12,13] In addition, target delineation with mpMRI is not trivial, which substantially lengthens MRI-guided radiotherapy procedures and may result in greater intrafraction motion. This is further limited by the magnet strength and experience of the imaging team.

A recent study demonstrated increased consensus of prostate specific membrane antigen (PSMA)-positron emission tomography (PET) volumes with histology compared with mpMRI for the delineation of intraprostatic GTVs, indicating that imaging with molecular targets increases imaging specificity.[14] Furthermore, GTVs derived from mpMRI significantly underestimated true tumor volumes compared to PSMA-PET. For intraprostatic radiotherapy boosting, imaging of molecular targets such as PSMA may therefore advantageously replace or be used in addition to conventional mpMRI and provides an additional biological characterization of malignant tissue for dose planning. However, PSMA-PET can intrinsically lead to GTV underestimation due to various technical aspects such as partial volume effects limiting image resolution.[15,16] In addition, PET-based target delineation suffers from the absence of integrated systems such as MRI-LINAC and MRI-US fusion. Conceptually, molecular MRI should provide improved imaging of tumoral features on a biological level over what is to date conventionally afforded by PET imaging. However, despite very extensive research in molecular MRI, especially with nano-particulate-based contrast agents, clinical translation is yet to be demonstrated.[17] This may be partly explained by the fact that most of the related research has to date focused on diagnostic applications as opposed to imaging and delineating primary lesions. Conceptually, the modular nature of nanoparticles enables for fine-tuning of the chemical design, therefore potentially affording excellent sensitivity and specificity for the targeted tumor biomarkers, which is key to minimizing the risk of overdiagnosis or underdiagnosis.[18] Conversely, iron-based MRI nanoparticulate contrast agents have well-established excellent safety profiles, paving the way to increased clinical use. The FDA has approved over the years many iron oxide nanoparticle-based MRI contrast agents, including most recently Magtrace for sentinel lymph node biopsy in breast cancer.[19]

Besides the imaging modality itself, a key requirement for molecular MRI is the selection of a biological target specific to the tumor. PSMA is often significantly overexpressed in PCa and as such has become the gold-standard target for molecular imaging of PCa.[20] Multiple PSMA ligands are now available for PET imaging with various FDA and EMA-approved PSMA-targeting probes demonstrating success in the clinic. However, loss of PSMA expression has been known to occur in neuroendocrine, androgen receptor-negative PCa, reducing the efficacy of PSMA-targeting probes in these cases. Furthermore, 5–10% of primary PCa or primary PCa lesions are PSMA-negative on PET.[21,22] Therefore, imaging of PSMA is not suitable for all patients, warranting the validation of additional imaging targets in PCa.[23]

Fibroblast activation protein (FAP) is an extracellular serine protease that is upregulated in stromal components of >90% of epithelial tumors but with low or undetectable expression in normal tissues.[24,25] Recent studies demonstrated that in a population of patients with PSMA-negative tumors, intermediate to high uptake of a ^{68}Ga-FAP inhibitor was observed in PCa.[26,27] In addition, FAP expression correlates with progression and worse prognosis.[24,28] Endothelial cells can also express FAP which contributes to the regulation of tumor angiogenesis, changes in capillary morphology, and microvascular reorganization.[29] Specifically, FAP has been found to be expressed by tumor endothelial cells during capillary formation but is absent in the mature endothelium.[30] Additionally, FAP expression correlates with a significantly increased density of microvessels.[31] As such, FAP is potentially a pan-cancer marker and a promising target for molecular imaging and therapy. FAP has been shown to be upregulated in PCa and is predominantly expressed in cancer-associated fibroblasts (CAFs) and reactive stromal cells adjacent to carcinoma cells.[32–34] Furthermore, FAP-specific PET imaging of malignancies with low PSMA expression demonstrated more precise results when compared to PSMA-PET.[35] Imaging of FAP in PCa has shown promise particularly in castrate-resistant prostate cancer (CRPC), with elevated FAP expression also observed in neuroendocrine
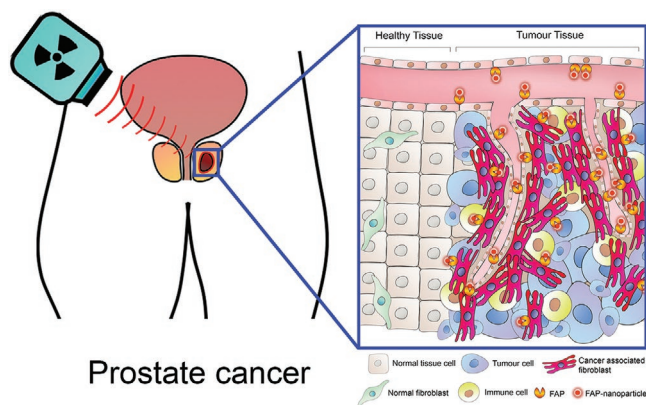
Figure 1. The binding of FAP-targeting nanoparticles within the complex tumor microenvironment. FAP is overexpressed in tumor stromal components such as cancer-associated fibroblasts and vasculature cells, adding to its suitability as a target for the imaging of solid tumors for the guidance of focal therapies such as radiotherapy.

prostate cancer (NEPC) and patients undergoing neoadjuvant androgen deprivation therapy (ADT).[36]

To date, the utility and significance of FAP-specific MRI are yet to be assessed. To address this question, here we report on benchmarking the performance of a FAP-targeted iron oxide nanoparticulate MRI agent against PSMA in the delineation of PCa in an orthotopic mouse model. As illustrated in **Figure 1**, we hypothesized that binding sites for FAP-targeting nanoparticles are enriched in the perivascular space within the tumor microenvironment, making FAP a good target for nanoparticle-based approaches. Our experimental approach builds on a previously reported FAP-ligand designed by ligating fragments of existing FAP ligands that were identified by molecular docking studies to contribute most prominently to the specificity and affinity of FAP binding.[37,38] The FAP and PSMA ligands were substituted from mannose in the FerroTrace iron oxide nanoparticulate agent that is presently undergoing clinical trial as a lymphotropic contrast agent. Using this novel imaging platform, we demonstrate that FAP MRI yields superior tumor contrast and coverage compared to PSMA in a preclinical model of PCa.

2. Experimental Section

2.1. Materials

The following chemicals were purchased and used as received without further purification. Trifluoroacetic acid, 1-ethyl-3-[3-dimethylaminopropyl]carbodiimide hydrochloride (EDC. HCl), N-hydroxysuccinimide (NHS), 4-morpholineethanesulfonic acid, 2-(N-morpholino)ethanesulfonic acid hydrate (MES hydrate), and 10× phosphate buffered saline were purchased from Sigma Aldrich. Acetone and dichloromethane (DCM) were purchased from Chem-Supply. FAP binding ligand was synthesized as previously described.[38] PSMA ligand Clu-CO-Lys-(tBu)$_3$ ester (CAS 1025796-31-9) was synthesized by Advanced Molecular Technologies (Scoresby, Victoria, Australia). The structures of the FAP and PSMA targeting ligands are displayed in Figure 3.

2.2. Analysis of FAP Expression in PCa

To evaluate FAP expression in normal prostates and prostate adenocarcinoma, normalized FAP RNAseq (expected count-deseq2+1) data was obtained from the Therapeutically Applicable Research to Generate Effect Treatments initiative (TARGET)/the Cancer Genome Atlas (TCGA)/Genotype-Tissue Expression (GTEx) dataset using the UCSC Xena platform (accessed 26/11/2021).[39] Corresponding patient prostate adenocarcinoma pathological T staging was obtained from the TCGA prostate adenocarcinoma (PRAD) data set (accessed 26/11/2021). Furthermore, immunohistochemistry staining of FAP in low- and high-grade prostate adenocarcinoma was obtained from the HPA059739 dataset deposited in the Human Protein Atlas (https://www.proteinatlas.org/ENSG00000078098-FAP/pathology/prostate+cancer#).[40]

2.3. Magnetic Nanoparticle Synthesis

The core maghemite iron oxide (γ-Fe$_2$O$_3$) nanoparticles were synthesized via co-precipitation of iron salts in aqueous solutions and subsequent controlled oxidation using iron nitrate as previously described.[41] To achieve in vivo stability, the nanoparticles were colloidally stabilized by block copolymers synthesized using reversible addition-fragment chain-transfer (RAFT) polymerization. The maghemite nanoparticles and RAFT block copolymer coating had been previously developed for the preparation of a lymphotropic MRI agent (FerroTrace, Ferronova) currently undergoing clinical trial.[41] Briefly, two types of block copolymer were attached to the nanoparticle surface: a stabilizing polymer (RAFT-5-MAPC2-15AAM-3PEO) and a targeting polymer with terminal FAP or PSMA ligands (RAFT-5MAPC2-70AAM-PSMA/FAP) in a mole ratio of 70% stabilizing to 30% targeting.

2.4. Preparation of RAFT-5MAPC2-15AAM-3PEO

Polymers were prepared based on a previously published procedure with modifications.[42] Methoxy triethylene glycol modified 2-{[butylsulfanyl)cabonothioyl]sulfanyl}propanoic acid (1.0 g), acrylamide (2.8 g), 4,4'-azobis(4-cyanovaleric acid) (0.050 g), dioxane (10 g), and water (10 g) were combined and dissolved before purging with nitrogen gas for 15 min and polymerizing at 70 °C for 2 h. The mixture was allowed to cool, opened to air, then (methacryloyloxy)-ethyl]phosphonic acid (2.5 g) and 4,4'-azobis(4-cyanovaleric acid) (0.050 g) were added to the reaction mixture. The mixture was purged with nitrogen gas for 15 min, then heated at 70 °C for 4 h. The polymer was precipitated in acetone, repurified, and collected by centrifugation.

2.5. Preparation of RAFT-5MAPC2-70AAM-PSMA/FAP Polymers

RAFT-COOH (2-(((butylthio)carbonothioyl)-thio)-propanoic acid) (0.2 g), 4,4'-azobis(4-cyanovaleric acid) (0.012 g), acrylamide (4.17 g), dioxane (7.8 g), and water (12.1 g) were combined and dissolved. The reaction was magnetically stirred at 70 °C

for 4 h in an inert atmosphere. The mixture was allowed to cool, opened to air, and [2-(methacryloyloxy)-ethyl]phosphonic acid (0.81 g) and 4,4'-azobis(4-cyanovaleric acid) (0.012 g) were added to the reaction mixture. The reaction was purged with nitrogen gas for 15 min before heating to 70 °C for 4 h under magnetic stirring. At this step, the RAFT-5MAPC2-70AAM polymer was precipitated in acetone, repurified, collected by centrifugation, and stored prior to conjugation with the FAP and PSMA ligands.

For preparing RAFT-5MAPC2-70AAM-PSMA, the tert-butyl ester groups of the PSMA ligand [Clu-CO-Lys-(tBu)$_3$ ester] were first removed using 20% trifluoroacetic acid (TFA) in dichloromethane (DCM). Briefly, 20 mg mL^{-1} PSMA in 20% TFA in DCM was mixed for 3 h at room temperature before vacuum drying. The residue was then dissolved in 10–20% aqueous acetic acid, transferred into a 50 mL falcon tube, and a two-fold volume of chloroform was added. The reaction was mixed thoroughly before the layers were allowed to separate and the bottom organic layer containing the protective groups and non-volatile by-products was removed using a needle and syringe. The extraction of the aqueous layer was repeated twice, and it was dried under high vacuum. The residue was dissolved in glacial acetic acid, made to shell-freeze, and lyophilized before use. The NH$_2$-derivatized FAP ligand was synthesized as previously described and used for the preparation of the RAFT-5MAPC2-70AAM-FAP.[31]

PSMA and FAP ligands were conjugated to the RAFT-5MAPC2-70AAM polymer using a carbodiimide coupling reaction. First, 200 mg of poly[[(methacryloyloxy)-ethyl]phosphonic acid]-*block*-poly(acrylamide), EDC.HCl (48 mg), and NHS (12 mg) were dissolved in 10 mL MES buffer (pH 5.0–5.5). The solution was mixed in a sonic bath for 10 min and the activated polymer was collected by precipitation in acetone followed by centrifugation. Second, FAP/PSMA ligands (12 mg) were dissolved in 100 µL DMSO and diluted to a total volume of 10 mL with 10X PBS buffer prior to addition to the activated polymer. The reaction mixture was stirred for 20 h. The conjugated polymer was purified using centrifugal filters with a 3 kDa molecular weight cut-off membrane. The product was diluted to a final concentration of 50 mg mL^{-1} and stored at 4 °C until further use.

2.6. Preparation of PSMA and FAP Nanoparticles

17 mg of RAFT-5MAPC2-15AAM-3PEO and 20 mg of RAFT-5MAPC2-70AAM-PSMA/FAP polymers were dissolved in 2 mL of water and the pH was adjusted to 4 using 0.1M NaOH. The maghemite nanoparticles (45 mg as dried weight) were added to the polymer solution under probe sonication. After mixing for 10 min, the pH was adjusted to 5.0 with NaOH (0.1M). Sonication was continued for a total of 30 min and the pH was further adjusted stepwise to 6.0 and 7.0. The nanoparticle suspension was purified using a centrifugal filter with a 100 kDa molecular weight cut-off membrane. Lastly, the nanoparticles were diluted with 3% saline to obtain a final concentration of 30 mg Fe mL^{-1} in 0.9% saline. An illustration of the PSMA/FAP nanoparticle preparation is shown in Figure 3a. For the preparation of non-targeted nanoparticles, the method described above was repeated except RAFT-5MAPC2-70AAM-PSMA/FAP was replaced by RAFT-5MAPC2-70AAM-COOH.

2.7. Nanoparticle Characterization

The morphology of the coated nanoparticles was studied using a transmission electron microscope (TEM; JEOL JEM-2100F-HR) equipped with a field emission gun operated at 200 kV. Images were recorded with a CCD Camera (Gatan Orius SC1000). Samples were prepared by placing a small drop of sample suspension in water onto a 200-mesh carbon-coated copper grid (ProSciTech) and subsequently evaporating water in the air. The mean diameter size by TEM was determined using an image processing package — Fiji (distribution of ImageJ). A total of 200 individual particles were measured from at least six different images at two different magnifications. Measurements were plotted as a histogram of the measured size of particle diameter (nm) against the frequency of measurement.

Dynamic light scattering (DLS) data were recorded on a Malvern Instruments Zetasizer Nano ZS at 25 °C. The hydrodynamic size of all nanoparticle suspensions was measured at a concentration of 0.1 mg Fe mL^{-1} and isotonic saline (0.9%) was used as suspending medium. Measurement duration was chosen as automatic.

Surface zeta potential data were acquired using the same instrumentation. The Smoluchowski method was used for the zeta potential measurements. The surface zeta potential of all nanoparticle suspensions was measured at a concentration of 1 mg Fe mL^{-1} and 10mM saline was used as the suspending medium.

2.8. Cancer Cell Lines and Culture Conditions

Cells were routinely cultured in RPMI-1640 medium (LNCaP and C32) (Gibco) or minimum essential medium (U87) (Gibco) supplemented with 10% fetal bovine serum (FBS) (Gibco) and 1% penicillin/streptomycin (Gibco) in a humidified atmosphere of 5% CO$_2$ at 37 °C. The medium was replaced every 2–3 days and cells were split once they reached 75–80% confluence using TrypLE Express (Gibco). LNCaP and U87 cells were gifted by Prof. Lisa Butler and Prof. Stuart Pitson, respectively.

2.9. Flow Cytometric Analysis of FAP Expression in U87 and C32 Cells

Cells were harvested from flasks using TrypLE Select (Thermo Fisher), washed in PBS, and resuspended in FACS buffer (1% bovine serum albumin (BSA) and 0.04% sodium azide in PBS). Staining for FAP was performed using either a one- or two-step process. For one-step staining, 90 µl of cells were incubated with 10 µl of anti-FAP-PE (clone 427819, R&D Systems) for 20 min at room temperature before washing with FACS buffer. For two-step staining, cells were incubated with mouse anti-FAP (clone 427819, R&D Systems) at a final concentration of 5 µg ml^{-1} for 20 min at room temperature and washed with FACS buffer, then incubated with goat anti-mouse

secondary antibody conjugated to AlexaFluor488 (Thermo Fisher #A-11029) at 10 µg mL^{-1} for 20 min at room temperature, then washed again in FACS buffer. Samples were acquired on an LSR Fortessa or Accuri C6 flow cytometer (both BD Biosciences). Analysis was performed using FCS Express V7 Flow Research Edition (De Novo Software, Pasadena, CA, USA).

2.10. Magnetic Nanoparticle In Vitro Binding Assay

To test the binding affinity of the PSMA/FAP nanoparticles, cellular binding in cells expressing the respective targets was measured in vitro. LNCaP cells were seeded in a T25 cell culture flask at a density of 1×10^6 cells per flask. C32 cells were seeded in a 6-well plate at a density of 3.5×10^5 cells per well in the complete cell culture medium as described above. The cells were placed in a 37 °C, 5% CO_2 incubator and allowed to adhere for 24 h. PSMA, FAP, and control unconjugated nanoparticle suspensions were prepared at a concentration of 0.150 mg Fe mL^{-1} in a cell culture medium. 6 mL of PSMA or control nanoparticle suspension was added to each flask containing adherent LNCaP cells or 1 mL of FAP and control nanoparticle suspension was added to each well containing adherent C32 cells. Three replicates were used to test each of the nanoparticle formulations. Cells were incubated with the nanoparticle suspensions for 24 h in an incubator at 37 °C in a 5% CO_2 humidified atmosphere. After incubation, cells were washed three times with PBS, detached using TrypLE Express and cell pellets were collected via centrifugation at 500g for 5 min. The cell pellets were washed twice with PBS and were dried at 60 °C overnight using a heating block. The dried cell pellets were digested with trace metal grade nitric and hydrochloric acid (1:1 ratio by volume). Digested samples were diluted with water to a total volume of 10 or 3 mL for LNCaP PSMA nanoparticles and C32 FAP nanoparticle samples, respectively. Iron concentration was measured by inductively coupled plasma mass spectroscopy (ICP-MS).

2.11. Preclinical Study in an Orthotopic Prostate Cancer Murine Model

All animal experiments were approved by the Animal Ethics Committee of the South Australian Health and Medical Research Institute (SAHMRI, approval number 450.19) and were conducted in accordance with Australian National Health and Medical Research Council (NHMRC) guidelines and the Animal Welfare Act and conformed to the Australian Code for the Care and Use of Animals for Scientific Purposes. Male NOD scid gamma (NSG) mice aged 6–8 weeks were bred and group-housed in a specific pathogen-free environment at the SAHMRI. Animals had ad libitum access to food and water and were clinically assessed daily. Mice were humanely euthanized via CO_2 inhalation to remove tissues.

Intraprostatic injection of cancer cells was performed as previously described.[43] Briefly, a lower midline incision was made, the bladder and prostate were externalized and 10 µL of RPMI-1640 containing 1×10^6 LNCaP-luciferase cells were injected into the anterior prostate using a precooled Hamilton syringe. To analyze tumor engraftment and growth, mice underwent weekly in vivo bioluminescence imaging (IVIS, Perkin Elmer), approximately 15–20 min post intraperitoneal injection with 150 mg kg^{-1} D-luciferin potassium salt.

2.12. Magnetic Resonance Imaging

After 5–6 weeks of tumor growth, mice were intravenously injected with 40 mg Fe kg^{-1} nanoparticles in up to 100 µL of saline. Healthy mice with no tumors were used as controls. Mice did not undergo baseline MRI scans prior to injection with particles. After a 24-h period, mice were anesthetized with 2% isoflurane in oxygen and were intraperitoneally injected with an overdose of pentobarbital prior to transcardial perfusion with 4% paraformaldehyde. Mice were postfixed in 4% paraformaldehyde prior to storage in PBS with 0.1% sodium azide. Mice underwent ex vivo T_2-weighted multiple graded echo sequence acquired using a 16.4 T Bruker Avance scanner (Bruker BioSpin, GmbH), with a 30 mm SAW coil (M2M Imaging, Brisbane, Australia) (repetition time 40 ms, echo time 10 ms, number of averages 1, slice thickness 0.1 mm) or fast low angle shot (FLASH) sequence using 9.4 T Bruker BioSpec scanner (Bruker BioSpin, GmbH, repetition time 50 ms, echo time 10 ms, number of averages 1, slice thickness 0.1 mm). At the completion of scans, tumors were excised and underwent FLASH scans using an 11.7 T Bruker Avance II scanner (Bruker BioSpin, GmbH, repetition time 100 ms, echo time 5.34 ms, number of averages 10, slice thickness 0.2 mm). All imaging was performed at room temperature. Horos was used to view scans (Horosproject.org, sponsored by Nimble Co LLC d/b/a Purview in Annapolis, MD USA).

Calculations of proportions of black pixels were based on protocols previously reported.[44,45] In brief, three regions of interest (ROI) were manually drawn over the prostate tumors in whole-body MR scans using ImageJ software (Bethesda, Maryland, USA).[46] Pixel intensity histograms were generated for each ROI. A low-intensity pixel threshold value was set, based on the visual analysis of threshold peaks.

Tumor T_2 maps were generated from 16.4 T and 9.4 T T_2-weighted MR images using an in-house code written in MATLAB (version 9.12.0 (R022a), The MathWorks, Inc., Natick, Massachusetts, United States). R_2 values were calculated from T_2 maps using a mono-exponential proton transverse relaxation method as previously published, using in-house code written in MATLAB.[47] In agreement with previously published studies, the authors found negligible differences in R_2 values between the two fields' strengths[48,49] and as such, they had been combined in the results. T_2 map tumor border ROIs were manually drawn throughout all tumor slices by an experienced MRI technician and the R_2 distribution was calculated for each tumor. The resulting R_2 histograms were plotted and the resulting Gaussian curves were used to calculate the change in mean R_2 and differences in area under the curve.

2.13. Haematoxylin and Eosin and Prussian Blue Staining

After ex vivo MR imaging, excised tumors, spleens, kidneys, and livers were mounted in paraffin and 4 µm thick sections

were stained with hematoxylin and eosin (H&E) or Prussian blue using standard protocols. Briefly, for Prussian blue staining sections were brought to distilled water and stained in an equal part mixture of potassium ferrocyanide and hydrochloric acid for 10 min, prior to washing in distilled water and counter+stain with neutral red stain. For H&E staining, slides were stained using Dako automated slide stainer (Agilent, United States). Briefly, slides were brought to distilled water prior to staining with hematoxylin for 1 min, bluing for 1 min, and eosin staining for 4.5 min. Images were processed using a Nanozoomer (Hamamatsu, Japan) and were visualized using ImageJ software (Bethesda, Maryland, United States). The percentage area of positive/blue Prussian Blue staining was calculated by setting color thresholds using ImageJ software.

2.14. Tissue Immunohistochemistry

4 µm paraffin-embedded tumor serial sections were used to compare Prussian blue staining with CD31, PSMA, and FAP immunohistochemistry. Staining was performed using a rabbit-specific HRP/DAB detection kit (Abcam) following the manufacturer's instructions, with modifications. Briefly, after hydration through a series of ethanol, sections were treated with hydrogen peroxide blocking for 10 min. Antigen retrieval was performed using pH 6 10 mM citrate buffer at 98 °C for 30 min and then incubated with 10% normal goat serum for 1 h for protein blocking. The sections were incubated overnight at 4 °C with anti-CD31 antibody (1:500, Abcam ab182981, EPR17259), anti-FAP antibody (1:300, Abcam ab28244), or anti-PSMA antibody (1:500, Abcam ab76104, EP3253). After washing, sections were treated with biotinylated antibody

and streptavidin peroxidase and developed with 3,3′-diaminobenzidine (DAB) (all provided in the kit). Images were processed using a Nanozoomer (Hamamatsu, Japan) and were visualized using ImageJ software (Bethesda, Maryland, USA).

The percentage area of positive staining was calculated by setting color thresholds using ImageJ. Entire images have been adjusted for brightness, contrast, and exposure, consistently between stains.

2.15. Statistical Analyses

Data are expressed as mean ± SEM in all cases. The significance of the results was determined by unpaired t-test or one-way ANOVA. Differences with a p-value of less than 0.05 were considered to be statistically significant. The relationship between FAP expression, PSA levels, and Gleason scores was assessed using simple linear regression. The relationship between the area of positive Prussian blue staining and CD31, FAP, and PSMA staining was assessed using Spearman rank correlations using GraphPad software.

3. Results

3.1. Human FAP Expression in the Normal Prostate and Prostate Adenocarcinoma

Analysis of available transcriptomic data showed a significant increase in FAP expression from normal prostate to adenocarcinoma ($p < 0.0001$) (**Figure 2**a). Further analysis comparing
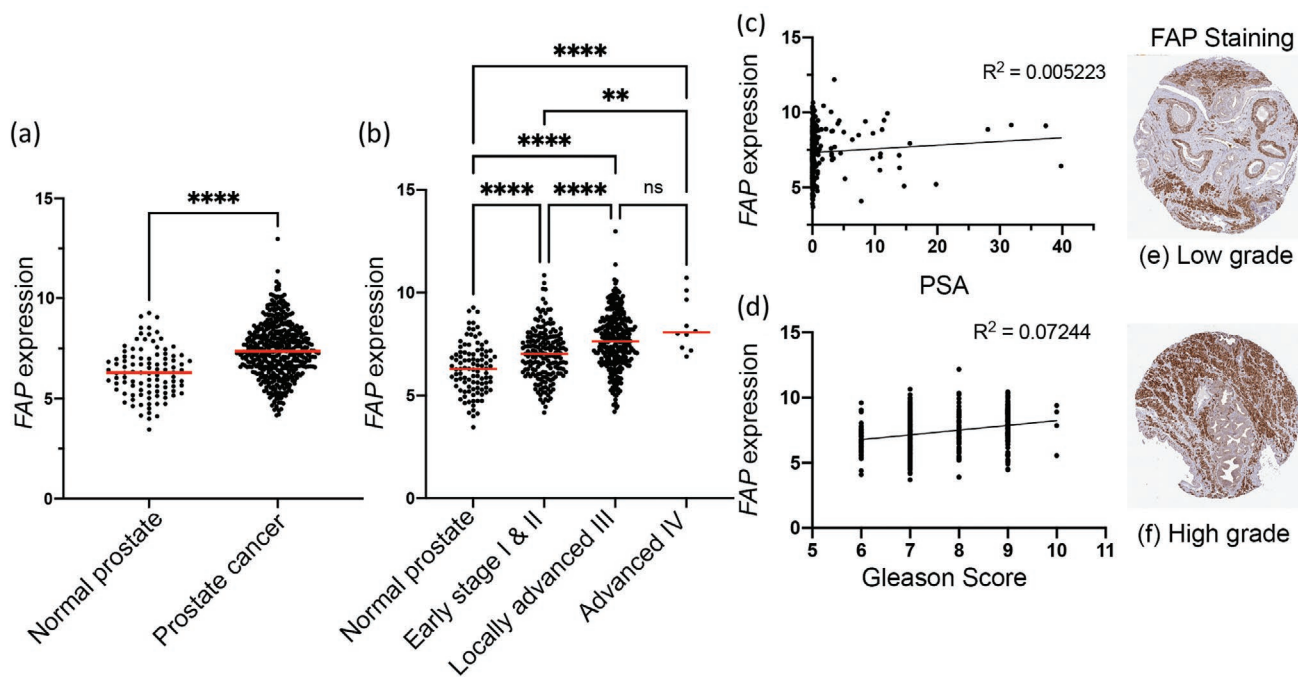

Figure 2. Transcriptomic analysis of FAP expression in clinical samples of prostate cancer. a) FAP gene expression values in prostate tumors compared with normal prostate obtained from the GTEX dataset. Red lines represent the medians of each group. b) FAP expression in relation to pathological T staging, c) PSA levels, and d) Gleason scores. e) FAP immunohistochemistry in biopsies of low-grade and f) high-grade prostate adenocarcinoma (images obtained from Human Protein Atlas).

the expression between pathological T stages demonstrated significant increases from normal prostate to early stage (I and II) ($p < 0.0001$) and to locally advanced (stage III) ($p < 0.0001$). However, there was no additional significant increase to advanced (IV) ($p > 0.05$) (Figure 2b). Linear correlation of Gleason score with FAP expression showed a weak positive relationship ($R^2 = 0.072$) (Figure 2d), whereas there was no correlation demonstrated with PSA ($R^2 = 0.005$) (Figure 2c). FAP expression was further demonstrated by FAP immunohistochemistry in biopsies of low- and high-grade prostate adenocarcinoma, obtained via the Human Protein Atlas (Figure 2e,f).

3.2. Characterization of Magnetic Nanoparticles

Iron oxide core nanoparticles with a polymeric coating consisting of target and stabilizing polymers were synthesized (**Figure 3**a). To assess the characteristics of the prepared PSMA, FAP, and control nanoparticles, a set of physicochemical characterizations was carried out. TEM images (Figure 3b,c), taken at 60 000× magnification, showed near-spherical, evenly dispersed FAP and PSMA nanoparticles even when dried on a carbon film. The mean diameter size of the particles measured by TEM was 16.2 ± 3.5 nm. DLS measurements of the hydrodynamic diameters confirmed that all coated nanoparticles have
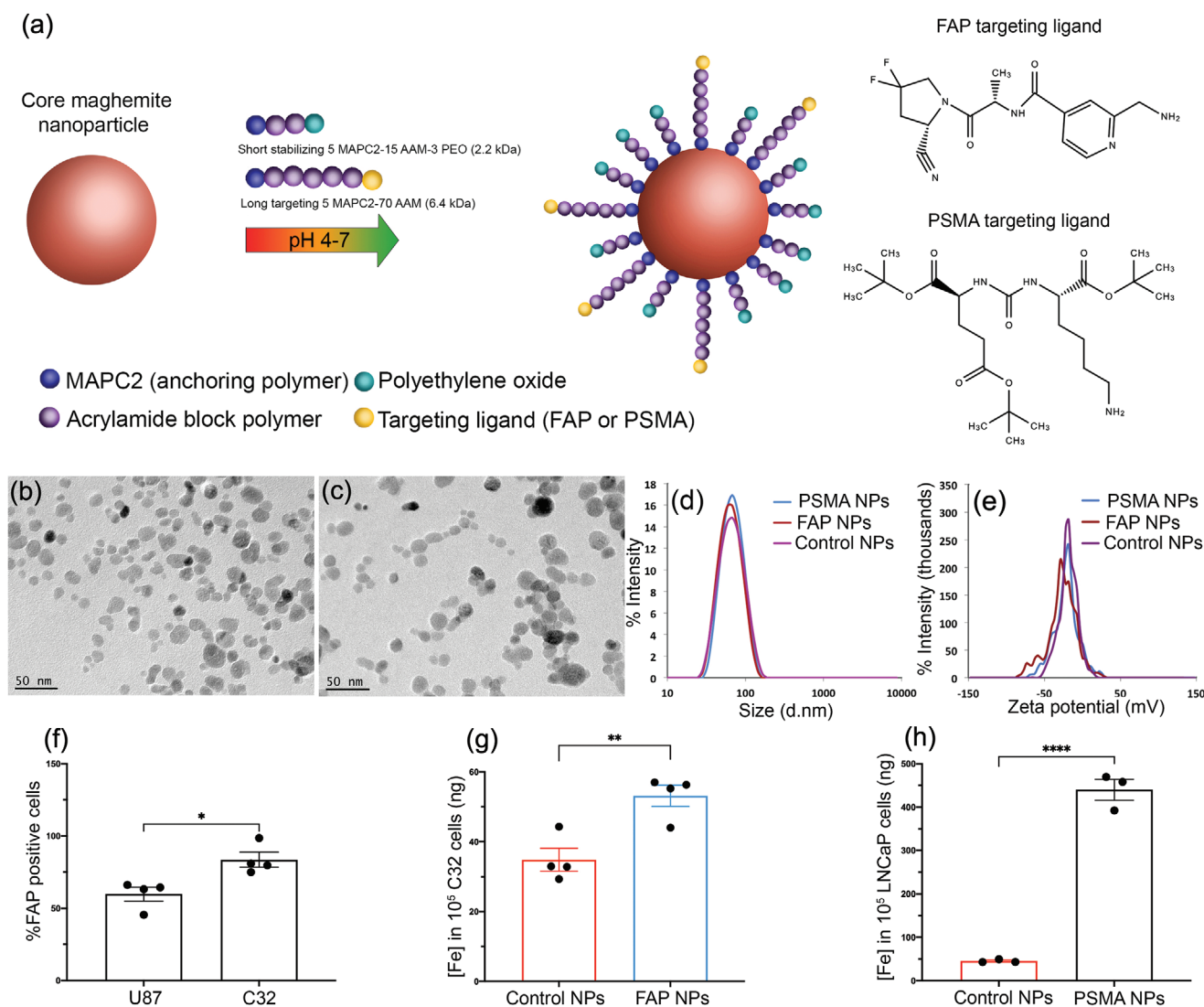

Figure 3. Preparation and characterization of FAP nanoparticles, PSMA nanoparticles, and non-targeted control nanoparticles. a) Schematic illustration of the preparation of FAP/PSMA nanoparticles. b,c) TEM images of FAP and PSMA nanoparticles at 60 000× magnification. d) Hydrodynamic size distribution by intensity and e) zeta potentials of FAP and PSMA and unconjugated control nanoparticles measured by dynamic light scattering. Evaluation of in vitro binding activity to cells expressing molecular PSMA and FAP targets. f) Flow cytometric analysis of the proportion of FAP-positive U87 and C32 cells. g) Cellular binding of FAP nanoparticles and non-targeted nanoparticles in FAP-positive C32 cells. h) Cellular binding of PSMA nanoparticles and non-targeted nanoparticles in PSMA-positive LNCaP cells. Data presented as mean ± SEM from 3–4 replicates per condition. PSMA versus non-targeted nanoparticles, $p < 0.0001$, $t(4) = 16.306$, FAP versus non-targeted nanoparticles, $p < 0.0001$, $t(4) = 18.892$, independent sample test.

an overall hydrodynamic size (z-average) of 60–65 nm when measured in physiological saline (Figure 3d). In addition, all DLS samples were characterized by a polydispersity index (PDI) of ≈0.1 which indicates a narrow size distribution of the samples. All nanoparticle suspensions were also characterized with similar zeta potential values ranging from an average of −17 to −20 mV (Figure 3e). The comparable surface changes and size distributions for the prepared FAP, PSMA, and control nanoparticle formulations are important for enabling meaningful comparison of the role of the targeting ligands.

3.3. In Vitro Binding Studies

The binding affinities of the prepared PSMA/FAP nanoparticles to the PSMA and FAP cell surface molecules were evaluated in vitro by comparing their binding to cancer cell lines which overexpress the molecules of interest. For nanoparticles used in biomedical applications, it is important to take into consideration the potential protein adsorption onto the nanoparticle's surface which can impact the binding activity, also known as the protein corona.[50,51] For taking the formation of the protein corona into account, cellular binding studies were performed in full cell culture media containing 10% serum and incubation time was prolonged to a 24-h period.

LNCaP cells have not been demonstrated to endogenously overexpress FAP, and therefore are not suitable for demonstrating in vitro binding of FAP-targeting nanoparticles. Previously, it has been demonstrated that U87 cells moderately endogenously express FAP.[52] Similarly, human melanoma cell lines have also previously demonstrated overexpression of FAP.[53] To determine the most suitable cell line for in vitro studies, we first compared FAP expression in U87 and C32 cell lines. Flow cytometric analysis of FAP expression demonstrated that C32 cells had ≈25% greater proportion of FAP-positive cells in contrast to U87 cells (Figure 3f), and as a result, the C32 cell line was chosen to perform in vitro binding studies. The targeted FAP nanoparticles had an uptake almost twice as high as the non-targeted nanoparticles (Figure 3g). The binding activity of PSMA nanoparticles was tested using the PSMA-expressing cell line LNCaP.[54] The results presented in Figure 3h indicated that the non-targeted nanoparticles had a much lower cellular binding compared to the targeted PSMA nanoparticles. Considering the similar physicochemical features of the PSMA/FAP nanoparticles when compared with the unconjugated control nanoparticles, these cellular binding data validate the chemical design and specific binding affinity of the conjugated nanoparticles to their respective targets. Note that there was no attempt to normalize the binding affinities of the FAP and PSMA nanoparticles to the respective receptors in each cell line used in the in vitro studies.

3.4. Magnetic Resonance Imaging of Orthotopic Prostate tumors

There was a significant increase in tumor contrast enhancement on T_2-W whole-body MRI after administration of both PSMA nanoparticles and FAP nanoparticles in mice bearing orthotopic LNCaP tumors compared to the unconjugated control nanoparticle group, as quantitatively demonstrated by the proportions of intratumoral black pixels (**Figure 4**, $p = 0.0358$ for PSMA nanoparticles and $p < 0.0001$ for FAP nanoparticles, $n = 3$–4 per group). FAP nanoparticle administration yielded ≈15% improvement in tumor contrast enhancement compared to PSMA nanoparticles ($p = 0.0004$, $n = 4$ per group). Administration of non-targeted control nanoparticles resulted in a
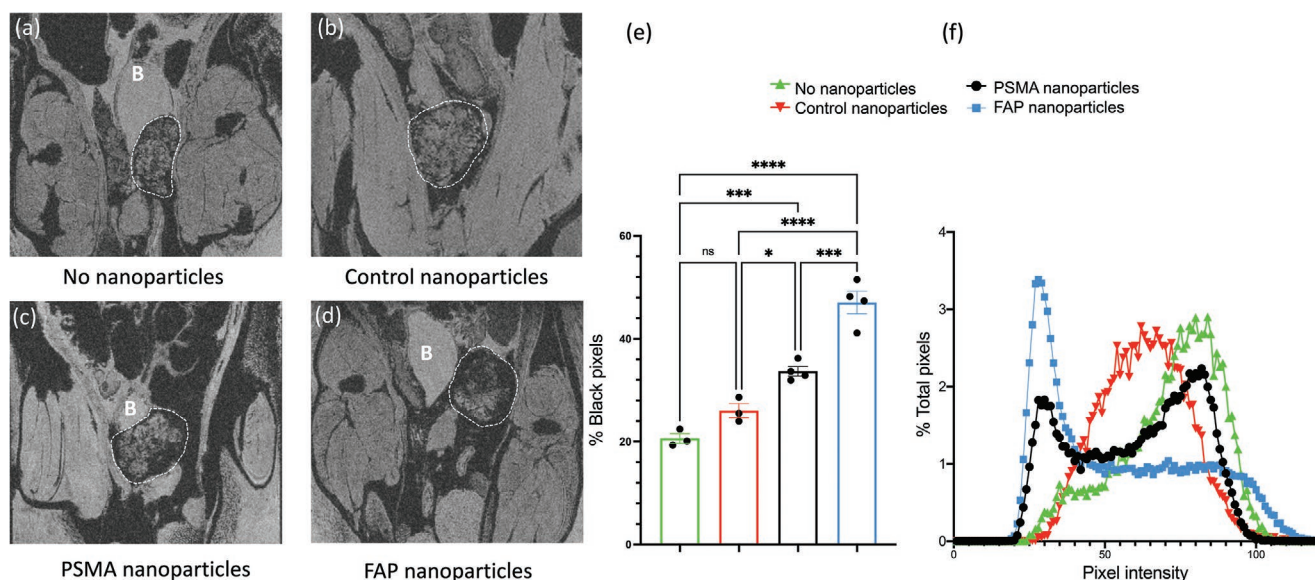

Figure 4. a–d) Representative coronal view of the lower abdomen in whole body T_2-W 16.4 T MRI of mice bearing orthotopic prostate tumors 24 h after intravenous injection with nanoparticles (40 mg Fe kg^{-1}) (representative images). PSMA nanoparticles and FAP nanoparticles enhance tumor contrast on MRI, relative to the administration of no nanoparticles and unconjugated control nanoparticles. B indicates bladder, white dotted border indicates orthotopic prostate tumor. e) Proportion of hypointense (black) pixels on T_2-W MRI in murine orthotopic prostate tumors 24 h after intravenous injection of FAP and PSMA nanoparticles (data presented as mean ± SEM). f) Representative total pixel distribution of analyzed ROIs.
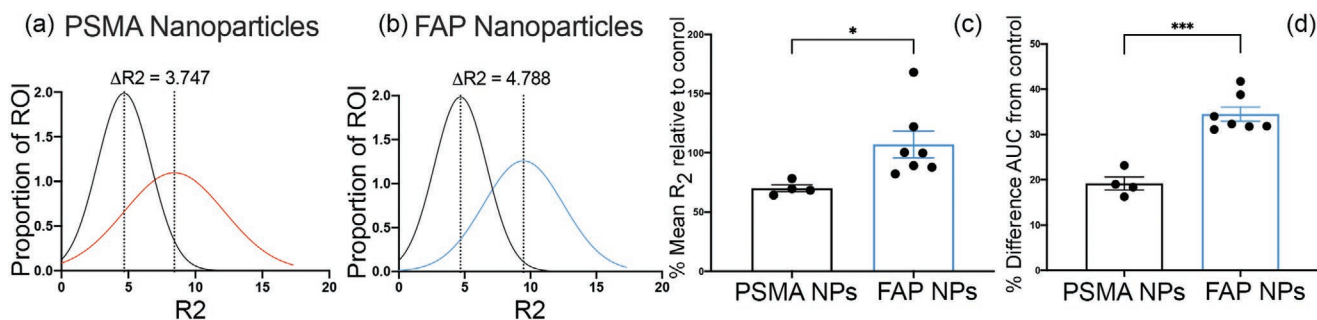
Figure 5. Assessment of change in R_2 values in prostate tumors relative to healthy control prostates. Representative R_2 traces of tumor borders after administration of a) PSMA nanoparticles (red line) and b) FAP nanoparticles (blue line) compared with healthy prostates (no tumor controls) with the same particles (black line). c) Percentage change in mean R_2 relative to healthy control, no tumor prostates with the same particles (70.14 vs 107.0, $p < 0.05$). d) Percentage difference of area under the curve of tumor R_2 distribution curves which are not covered by the control curve (19.21% vs 34.52%, $p < 0.001$).

modest, nonsignificant increase in tumor contrast relative to the no nanoparticle control group ($p = 0.2615$, $n = 3$ per group).

To better assess the potential for tumor delineation, changes in R_2 distribution between prostate tumors and healthy prostates were examined. Specifically, tumor borders were compared against the healthy prostate in animals administered with the same particles. Due to the overgrowth of LNCaP tumors in the prostate, these calculations were performed using separate animals. PSMA and FAP nanoparticles induced a shift in contrast in tumors (**Figure 5**a,b), relative to control prostates, respectively. The percentage change in mean R_2 relative to the healthy control with the same particles was greater in FAP nanoparticles (mean change 107%) than in PSMA nanoparticles (mean change 70%) (Figure 5c, $p < 0.05$). More specifically, FAP nanoparticles had a greater percentage difference in area under the curve relative to the healthy control prostate in contrast to PSMA nanoparticles (Figure 5d, $p < 0.001$). Pixels in this area under the curve which is not covered by the control may contribute towards the change in contrast required for tumor delineation within the healthy prostate.

3.5. Distribution of Magnetic Nanoparticles in Tissues

To examine the intratumoral distribution of non-heme iron after the administration of the PSMA/FAP nanoparticles, Prussian blue staining was performed on sections of LNCaP orthotopic prostate tumors and normal prostates (**Figure 6**a). No positive staining was observed in normal prostate sections. The absence of Prussian blue staining in sections of normal prostate for mice administrated with control, FAP, and PSMA nanoparticles confirmed the lack of significant nanoparticle accumulation in the absence of orthotopic tumors. LNCaP tumors also showed minimal positive basal staining. In agreement with the MRI data, modest Prussian blue staining was observed after the administration of control nanoparticles. On the other hand, LNCaP tumors showed significant positive staining after the administration of PSMA and FAP nanoparticles, of which the staining was concentrated on the tumor periphery. Both PSMA and FAP nanoparticles demonstrated heterogenous intermittent intratumoral staining, some of which was suggestive of blood vessel staining, the frequency of which was greater in FAP nanoparticles compared to PSMA nanoparticles.

To better understand the distribution of the nanoparticles within tumors, positive Prussian blue stained areas were correlated with positive areas for CD31 or PSMA or FAP (Figure 6b–e and representative images Figure 6f–h,j–l). It was found that Prussian blue staining as a result of FAP nanoparticles correlated more strongly with the positive area of CD31 staining compared to PSMA-targeted particles (Figure 6b,d). Furthermore, FAP nanoparticles had a stronger correlation with Prussian blue staining and positive staining of FAP, when compared with PSMA particles Prussian blue staining and PSMA expression (Figure 6c,e). These relationships may be explained by the tumoral distribution of FAP and PSMA expression, as PSMA is expressed by LNCaP cells and therefore throughout the tumors, in contrast to FAP, which is primarily expressed by stromal components including perivascular regions. To confirm the distribution of the iron oxide nanoparticles and their effect on MRI, high-resolution MR imaging of resected tumors treated with either FAP nanoparticles or PSMA nanoparticles was performed. Preferential contrast enhancement was observed at the tumor peripheries, in contrast to homogenous contrast enhancement throughout the tumors (Figure 6i,m), suggesting preferential accumulation of the nanoparticles to the highly vascularized tumor periphery, in qualitative agreement with the Prussian blue staining data. Higher densities of vascular structures at the periphery of such orthotopic models have been previously demonstrated.[55]

Finally, Prussian blue staining was performed to assess the distribution of iron oxide nanoparticles in the kidney, liver, and spleen in orthotopic tumor mice (**Figure 7**). Through visual assessment, there was no increase in Prussian blue staining in the spleen and kidneys in all nanoparticle groups when compared to the no particle control. As expected, we observed a marginal increase in Prussian blue staining in the liver compared to the no nanoparticle control, which was consistent among all nanoparticles. Furthermore, to preliminarily assess potential acute toxicities, H&E staining was performed on the kidneys, liver, and spleen of LNCaP tumor-bearing mice (Figure 7). No changes in tissue morphology were observed across the kidneys, liver, and spleen in a control, PSMA, and FAP-targeting nanoparticles, when compared to the no nanoparticle control.
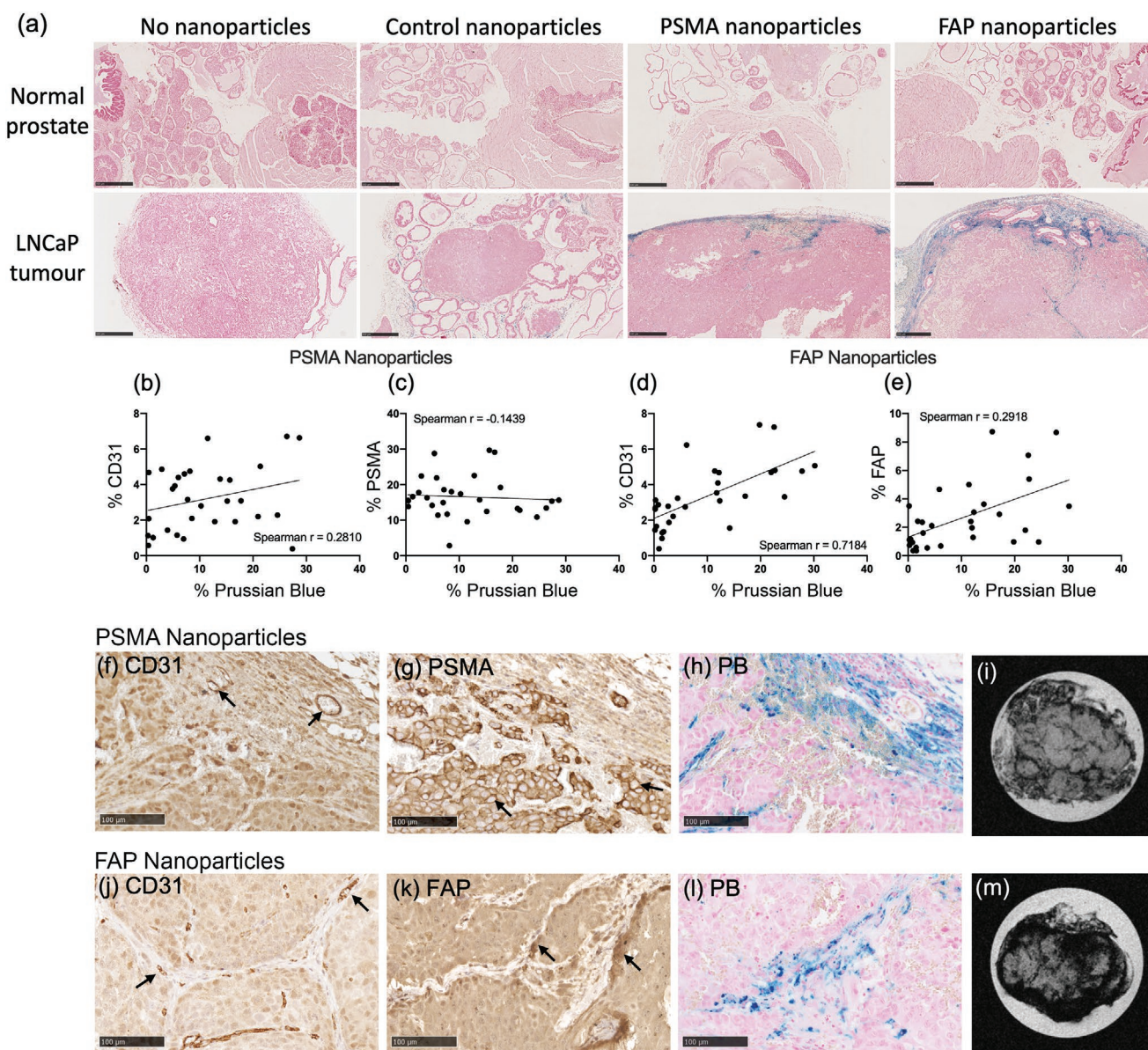
**ADVANCED
SCIENCE NEWS**

www.advancedsciencenews.com

NANO · MICRO

small

www.small-journal.com

Figure 6. a) Representative images of Prussian blue staining of cross sections of normal prostates and orthotopic prostate tumors after intravenous injection with no nanoparticles, control nanoparticles, PSMA nanoparticles, and FAP nanoparticles (all nanoparticles 40 mg Fe kg^{-1}). All images are at 5× magnification, scale bar is 500 µm. b–e) Correlation of sequential Prussian blue staining with immunohistochemistry analysis of CD31, PSMA, and FAP expression in LNCaP tumors. b,c) show the correlation of colocalization of PSMA nanoparticles with the expression of CD31 and PSMA, with representative images shown in (f–h). d,e) show the correlation of colocalization of FAP nanoparticles with the expression of CD31 and FAP, representative images shown in (j–l). Representative images are at 15× magnification, scale bar is 100 µm. Arrows indicate examples of positive staining. The relationship between the positive Prussian blue area and PSMA, FAP, or CD31 positive area is assessed by Spearman rank correlation (shown on the graph). i,m) High-resolution ex vivo T$_2$-W 11.7 T MRI of murine LNCaP tumors 24 h after intravenous injection of PSMA and FAP nanoparticles (representative images).

4. Discussion

Focal boost therapies for PCa aim to selectively eliminate dominant intraprostatic malignant lesions whilst sparing surrounding off-target tissues, and in doing so achieve oncological outcomes similar to those afforded by whole gland treatment but with reduced adverse effects. To enable effective focal treatment with contemporary treatment approaches including image-guided radiotherapy, target volumes and safety margins must be precisely defined. Current MRI techniques such as mpMRI have yielded promising performance in providing treatment guidance but are susceptible to underestimation of the true tumor volume[56] and are time and resource-demanding. This may be improved through the utilization of molecular MRI targeting tumor markers.

Targeting of the pan-cancer marker FAP has practice-redefining potential in the treatment of solid tumors such as PCa, through improved boundary delineation, possibly enabling the
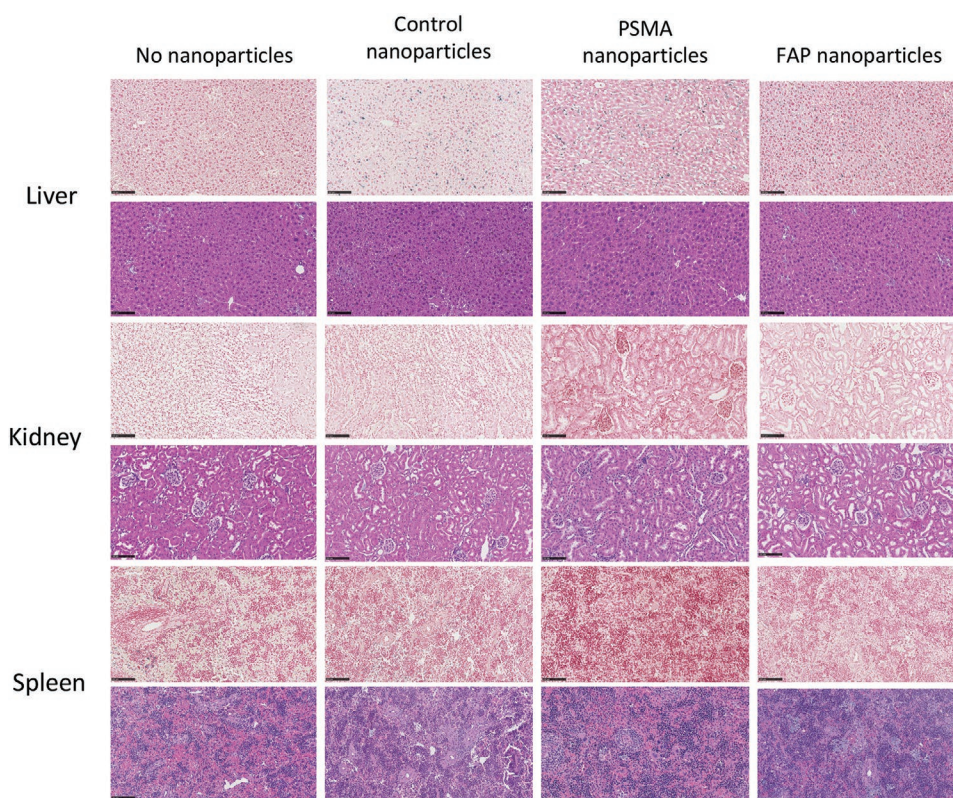
Figure 7. Haematoxylin and eosin (bottom row) and Prussian blue (top row) staining of liver, kidney, and spleen of orthotopic LNCaP tumor mice, 24 h after intravenous injection with nanoparticles. No changes in H&E staining were identified in the liver, kidney, and spleen in all nanoparticle groups, compared to the no nanoparticle control. The kidneys and spleen did not show an increase in Prussian blue staining, relative to the no particle control, however, a slight increase was observed in the liver, which was consistent across all nanoparticles. All images are at 20× magnification, scale bar is 100 µm.

use of focal lesion ablative microboosts. FAP is predominantly expressed on CAFs which reside in the tumor stroma, as well as in perivascular and endothelial cells and expression is present in virtually all solid tumors.[57,58]

Unlike cancer cells, CAFs are not undergoing mutation, adding to the promising targeting qualities of FAP.[38,59,60] Human prostate tumors can have over 50% stromal component, which can be greater in cases of desmoplastic reaction.[26] As such, targeting the tumor stroma may provide increased imaging sensitivity and contrast agent retention at the intraprostatic target site compared with the targeting of tumor cells themselves. PCa metastases have also been demonstrated to be FAP positive, possibly enabling focal metastatic lesion ablative treatment. In support of this train of thought, pilot studies using PSMA-PET have shown efficacy in image-guided radiotherapy of metastases for the treatment of oligorecurrent PCa.[61] In another study, 1.5T MRI-guided stereotactic body radiotherapy by LINAC guided by PSMA-PET produced encouraging oncological and tolerability results in the management of oligometastatic castration-sensitive prostate cancer.[62] Recently, FAP-targeted PET has demonstrated fair to good interobserver agreement rates in the detection of organ and lymph node metastases across a variety of tumor types.[63] There are yet to be clinical studies investigating the use of molecular MRI contrast agents in image-guided radiotherapy. FAP-targeted MRI-guided radiotherapy may also prove beneficial in palliative radiotherapy, particularly in reducing pain arising from PCa bone metastases, leading to improved quality of life.[64]

FAP-specific imaging may be most beneficial in late-stage and clinically aggressive cancers, in which FAP expression can be more pronounced than PSMA, and in cases with doubtful lesions, therapy failure, and/or PSMA downregulation or negative disease.[35,65] Patients undergoing long-term ADT may have a decreased detection sensitivity on PSMA imaging due to the downregulation of receptors, although this issue may be mitigated by ceasing ADT prior to imaging studies.[66] Current literature suggests that short-term ADT upregulates PSMA, suggesting that PSMA-targeted imaging is suitable in these patients.

Although various FAP and PSMA-specific PET tracers are being actively developed, PET imaging lacks the resolution that is optimal for focal radiotherapy. MR boasts superior soft tissue contrast, visualization of organ movement, and the ability to monitor changes in tumor and tissue physiology, enabling improved adaptation of target volumes between radiotherapy treatment fractions.[67] However, the interpretation of PCa mpMRI is susceptible to significant variability as demonstrated by discordance in prostate imaging reporting and data system (PIRADS) score assignment and cancer yield by radiologists.[68] MRI provides high-resolution 3D morphological information which can be enhanced with the use of magnetic core nanoparticles which cause hypointense signals (darkening) on

MR imaging by decreasing the relaxation times of protons in surrounding water molecules. This exogenous contrast of the tumor may lead to decreased inter-observer variability of GTV delineation. The utilization of FAP or PSMA-targeted MRI may also improve the delineation of low-grade diseases, such as Gleason 3+3 cancers which are often missed on MRI.[69] Furthermore, it was found that T_2-weighted MRI underestimated GTVs, longest axis, and pathological tumor extent in nearly every case. Furthermore, cellular composition, density, and interstitial stromal space have an effect on diffusion-weighted imaging (DWI) and derived apparent diffusion coefficient (ADC) maps, which may contribute to the underestimation of GTVs.[70]

Despite its conceptual benefits in regard to image-guided treatment, the clinical feasibility of molecular MRI remains to be demonstrated. PET imaging is the current gold standard for receptor-based molecular imaging largely due to its high sensitivity ($\approx10^{-12}$ M), which is greatly superior to MRI ($\approx10^{-4}$ M).[71] The detection threshold of iron nanoparticles using MRI is affected by numerous parameters including field strength, signal-to-noise ratio, pulse sequence, particle design, and voxel size.[72] However, various studies have demonstrated the ability to track iron nanoparticle-labeled stem cells using MRI in mice and humans to a detection limit of a few hundred cells.[72] Longitudinal and or the comparison of pre- and post-contrast imaging may aid in mitigating MRI sensitivity limitations. Furthermore, several research groups and scanner manufacturers are developing and optimizing specially designed pulse sequences to exploit and selectively detect iron nanoparticle susceptibility. This includes sequences such as magnetization-prepared rapid gradient-echo (MP-RAGE) and ultrashort echo time (UTE) which have been shown to provide high-contrast images of iron nanoparticles up to 7.5 and 45 mM, respectively.[73] The availability of the target tumor biomarker should also be considered as the relatively high dose of nanoparticles required to achieve useful contrast might exceed the saturation threshold, and this point warrants further investigation in a more advanced preclinical model. Finally, while MRI lacks sensitivity compared to PET, it exceeds PET in spatial resolution (<1 mm, 2–6 mm, respectively) and provides superior anatomical information. We anticipate that these factors combined with purpose-designed particles will be beneficial for the planning of radiotherapy treatment volumes as, in contrast to using PET, additional imaging may not be required.

In this study, we designed, synthesized, and characterized FAP and PSMA-targeted iron oxide nanoparticles for molecular MRI and comparatively assessed imaging performance in vivo in an orthotopic model of prostate cancer. As murine FAP shares 89% of the human FAP amino acid sequence, the FAP-targeting nanoparticles used in this study are suitable for both species.[74,75] To our knowledge, this is the first report describing the use of FAP-specific MRI. The ligand-targeted nanoparticles are based on a lymphotropic agent that has been validated in a large animal model and presently undergoing clinical trial (ACTRN12620000831987). The design relies on targeting and stabilizing block copolymers of different lengths that enable efficient targeting using small molecule ligands as shown in the excellent binding affinity observed here in vitro with PSMA and FAP expressing cells.

Both FAP and PSMA-targeted nanoparticles yielded improved tumor accumulation as shown by the increase in MRI contrast in orthotopic tumor-bearing mice compared to non-targeted nanoparticles. Interestingly, FAP-targeted MRI outperformed MRI-targeting PSMA in contrast enhancement and delineation of orthotopic LNCaP tumors. The LNCaP tumor model was selected for this study as it is commonly used for preclinical studies of PSMA-specific diagnostic and therapeutic agents. Additionally, the expression of FAP in the stroma of orthotopic LNCaP tumors has been previously demonstrated as indicated by colocalization of both FAP and α-smooth muscle actin.[76] The excellent imaging performance of the FAP nanoparticles observed here could be explained by the distribution of FAP expression, which predominantly occurs in the stroma and vasculature, and might therefore be more accessible to nanoparticulate imaging agents than markers expressed by tumor cells (Figure 1). Not surprisingly, the enhanced contrast associated with the presence of the iron oxide nanoparticles was found to be more pronounced at the periphery of the orthotopic tumors. As expected, unconjugated nanoparticles provided a modest improvement in the MRI contrast. Non-specific accumulation of nanoparticles within solid tumors is typically observed in preclinical mouse models, although the precise mechanisms are still controversial.[77] Prussian Blue staining confirmed that non-specific uptake was not associated with the hemorrhagic phenotype of the LNCaP tumors. Enhanced tumor contrast on MRI has also been confirmed in several clinical trials for various dextran-coated iron oxide nanoparticles.[78] The ongoing NCT04682847 trial investigates the use of ferumoxytol, a non-targeted iron oxide nanoparticle, in MRI-LINAC treatment of hepatic cancer.

Considering the pan-cancer nature of FAP expression in the stroma of solid tumors, FAP-specific MRI with rationally designed iron oxide nanoparticles may prove useful in the delineation of other solid tumors such as gastrointestinal and brain cancer. FAP-specific MRI warrants further investigation, especially in combination with highly conformal radiotherapy such as MRI-LINAC. It could also advantageously guide radiotherapy with proton therapies, thereby fully harnessing the precise dose deposition afforded by this technique.[79]

Supporting Information

Supporting Information is available from the Wiley Online Library or from the author.

Acknowledgements

Conflict of Interest

Author Contributions

Data Availability Statement

The data that support the findings of this study are available from the corresponding author upon reasonable request.

Keywords

[1] H. Sung, J. Ferlay, R. L. Siegel, M. Laversanne, I. Soerjomataram, A. Jemal, F. Bray, *Ca-Cancer J. Clin.* **2021**, *71*, 209.

[2] C. D. Goodman, H. Fakir, S. Pautler, J. Chin, G. S. Bauman, *Adv. Radiat. Oncol.* **2020**, *5*, 212.

[3] G. A. Viani, E. J. Stefano, S. L. Afonso, *Int. J. Radiat. Oncol., Biol., Phys.* **2009**, *74*, 1405.

[4] C. G. Mazariego, S. Egger, M. T. King, I. Juraskova, H. Woo, M. Berry, B. K. Armstrong, D. P. Smith, *BMJ* **2020**, *371*, m3503.

[5] R. Matta, C. R. Chapple, M. Fisch, A. Heidenreich, S. Herschorn, R. T. Kodama, B. F. Koontz, D. G. Murphy, P. L. Nguyen, R. K. Nam, *Eur. Urol.* **2019**, *75*, 464.

[6] E. Arrayeh, A. C. Westphalen, J. Kurhanewicz, M. Roach, A. J. Jung, P. R. Carroll, F. V. Coakley, *Int. J. Radiat. Oncol., Biol., Phys.* **2012**, *82*, 787.

[7] D. Pucar, H. Hricak, A. Shukla-Dave, K. Kuroiwa, M. Drobnjak, J. Eastham, P. T. Scardino, M. J. Zelefsky, *Int. J. Radiat. Oncol., Biol., Phys.* **2007**, *69*, 62.

[8] J. R. Murray, A. C. Tree, E. J. Alexander, A. Sohaib, S. Hazell, K. Thomas, R. Gunapala, C. C. Parker, R. A. Huddart, A. Gao, L. Truelove, H. A. Mcnair, I. Blasiak-Wal, N. M. Desouza, D. Dearnaley, *Int. J. Radiat. Oncol., Biol., Phys.* **2020**, *106*, 715.

[9] L. G. W. Kerkmeijer, V. H. Groen, F. J. Pos, K. Haustermans, E. M. Monninkhof, R. J. Smeenk, M. Kunze-Busch, J. C. J. De Boer, J. Van Der Voort Van Zijp, M. Van Vulpen, C. Draulans, L. Van Den Bergh, S. Isebaert, U. A. Van Der Heide, *J. Clin. Oncol.* **2021**, *39*, 787.

[10] S. Ghai, A. Finelli, K. Corr, R. Chan, S. Jokhu, X. Li, S. Mccluskey, A. Konukhova, E. Hlasny, T. H. Van Der Kwast, P. F. Incze, A. R. Zlotta, R. J. Hamilton, M. A. Haider, W. Kucharczyk, N. Perlis, *Radiology* **2021**, *298*, 695.

[11] E. Walser, A. Nance, L. Ynalvez, S. Yong, J. S. Aoughsten, E. J. Eyzaguirre, S. B. Williams, *J. Vasc. Interventional Radiol.* **2019**, *30*, 401.

[12] B. G. Muller, J. H. Shih, S. Sankineni, J. Marko, S. Rais-Bahrami, A. K. George, J. J. M. C. H. De La Rosette, M. J. Merino, B. J. Wood, P. Pinto, P. L. Choyke, B. Turkbey, *Radiology* **2015**, *277*, 741.

[13] H. U. Ahmed, A. El-Shater Bosaily, L. C. Brown, R. Gabe, R. Kaplan, M. K. Parmar, Y. Collaco-Moraes, K. Ward, R. G. Hindley, A. Freeman, A. P. Kirkham, R. Oldroyd, C. Parker, M. Emberton, *Lancet* **2017**, *389*, 815.

[14] A. S. Bettermann, C. Zamboglou, S. Kiefer, C. A. Jilg, S. Spohn, J. Kranz-Rudolph, T. F. Fassbender, P. Bronsert, N. H. Nicolay, C. Gratzke, M. Bock, J. Ruf, M. Benndorf, A. L. Grosu, *Radiother. Oncol.* **2019**, *141*, 214.

[15] M. Piert, P. R. Shankar, J. Montgomery, L. P. Kunju, V. Rogers, J. Siddiqui, T. Rajendiran, J. Hearn, A. George, X. Shao, M. S. Davenport, *EJNMMI Res.* **2018**, *8*, 23.

[16] M. Piert, H. Park, A. Khan, J. Siddiqui, H. Hussain, T. Chenevert, D. Wood, T. Johnson, R. B. Shah, C. Meyer, *J. Nucl. Med.* **2009**, *50*, 1585.

[17] N. Schleich, F. Danhier, V. Préat, *J. Controlled Release* **2015**, *198*, 35.

[18] M. Barani, F. Sabir, A. Rahdar, R. Arshad, G. Z. Kyzas, *Nanomaterials* **2020**, *10*, 1696.

[19] S. Shams, K. Lippold, J. U. Blohmer, R. Röhle, F. Kühn, M. M. Karsten, *Ann. Surg. Oncol.* **2021**, *28*, 3232.

[20] K. Bouchelouche, P. L. Choyke, J. Capala, *Discovery Med.* **2010**, *9*, 55.

[21] L. Budäus, S.-R. Leyh-Bannurah, G. Salomon, U. Michl, H. Heinzer, H. Huland, M. Graefen, T. Steuber, C. Rosenbaum, *Eur. Urol.* **2016**, *69*, 393.

[22] T. Maurer, J. E. Gschwend, I. Rauscher, M. Souvatzoglou, B. Haller, G. Weirich, H.-J. Wester, M. Heck, H. Kübler, A. J. Beer, M. Schwaiger, M. Eiber, *J. Urol.* **2016**, *195*, 1436.

[23] J. J. Tosoian, M. A. Gorin, S. P. Rowe, D. Andreas, Z. Szabo, K. J. Pienta, M. G. Pomper, T. L. Lotan, A. E. Ross, *Clin. Genitourin. Cancer* **2017**, *15*, 65.

[24] F. Zi, J. He, D. He, Yi Li, Li Yang, Z. Cai, *Mol. Med. Rep.* **2015**, *11*, 3203.

[25] P. Garin-Chesa, L. J. Old, W. J. Rettig, *Proc. Natl. Acad. Sci. U. S. A.* **1990**, *87*, 7235.

[26] H. M. Hintz, J. P. Gallant, D. J. Vander Griend, I. M. Coleman, P. S. Nelson, A. M. Lebeau, *Clin. Cancer Res.* **2020**, *26*, 4882.

[27] F. Khreish, F. Rosar, C. Kratochwil, F. L. Giesel, U. Haberkorn, S. Ezziddin, *Eur. J. Nucl. Med. Mol. Imaging* **2020**, *47*, 2040.

[28] F. Liu, Li Qi, B. Liu, J. Liu, H. Zhang, D. Che, J. Cao, J. Shen, J. Geng, Yi Bi, L. Ye, Bo Pan, Y. Yu, *PLoS One* **2015**, *10*, 0116683.

[29] R. Aimes, A. Zijlstra, J. Hooper, S. Ogbourne, M-Le Sit, S. Fuchs, D. Gotley, J. Quigley, T. Antalis, *Thromb. Haemostasis* **2003**, *89*, 561.

[30] L. Xin, J. Gao, Z. Zheng, Y. Chen, S. Lv, Z. Zhao, C. Yu, X. Yang, R. Zhang, *Front. Oncol.* **2021**, *11*, 648187.

[31] Li-M Gao, F. Wang, Y. Zheng, Z.-Z. Fu, L. Zheng, L.-L. Chen, *Pathol. Oncol. Res.* **2019**, *25*, 369.

[32] E. Giannoni, F. Bianchini, L. Masieri, S. Serni, E. Torre, L. Calorini, P. Chiarugi, *Cancer Res.* **2010**, *70*, 6945.

[33] A. M. Lebeau, W. N Brennen, S. Aggarwal, S. R. Denmeade, *Mol. Cancer Ther.* **2009**, *8*, 1378.

[34] J. A. Tuxhorn, G. E. Ayala, M. J. Smith, V. C. Smith, T. D. Dang, D. R. Rowley, *Clin. Cancer Res.* **2002**, *8*, 2912.

[35] K. Kessel, R. Seifert, M. Weckesser, M. Boegemann, S. Huss, C. Kratochwil, U. Haberkorn, F. Giesel, K. Rahbar, *Ann. Nucl. Med.* **2022**, *36*, 293.

[36] C. Kesch, L. Yirga, K. Dendl, A. Handke, C. Darr, U. Krafft, J. P. Radtke, S. Tschirdewahn, T. Szarvas, L. Fazli, M. Gleave, F. L. Giesel, U. Haberkorn, B. Hadaschik, *Eur. J. Nucl. Med. Mol. Imaging* **2021**, *49*, 385.

[37] R. Mukkamala, S. D. Lindeman, K. A. Kragness, I. Shahriar, M. Srinivasarao, P. S. Low, *J. Mater. Chem. B* **2022**, *10*, 2038.

[38] J. Roy, S. U. Hettiarachchi, M. Kaake, R. Mukkamala, P. S. Low, *Theranostics* **2020**, *10*, 5778.

[39] M. J. Goldman, B. Craft, M. Hastie, K. Repečka, F. Mcdade, A. Kamath, A. Banerjee, Y. Luo, D. Rogers, A. N. Brooks, J. Zhu, D. Haussler, *Nat. Biotechnol.* **2020**, *38*, 675.

[40] M. Uhlén, L. Fagerberg, B. M. Hallström, C. Lindskog, P. Oksvold, A. Mardinoglu, Å. Sivertsson, C. Kampf, E. Sjöstedt, A. Asplund, I. Olsson, K. Edlund, E. Lundberg, S. Navani, C. Al-K Szigyarto, J. Odeberg, D. Djureinovic, J. O. Takanen, S. Hober, T. Alm, P.-H. Edqvist, H. Berling, H. Tegel, J. Mulder, J. Rockberg, P. Nilsson, J. M. Schwenk, M. Hamsten, K. Von Feilitzen, M. Forsberg, et al., *Science* **2015**, *347*, 1260419.

[41] G. Krishnan, A. Cousins, N. Pham, V. Milanova, M. Nelson, S. Krishnan, A. Shetty, N. Van Den Berg, E. Rosenthal, S. Krishnan, P.-J. Wormald, A. Foreman, B. Thierry, *Nanomedicine* **2022**, *42*, 102546.

[42] N. S. Bryce, B. T. T. Pham, N. W. S. Fong, N. Jain, Eh. H Pan, R. M. Whan, T. W. Hambley, B. S. Hawkett, *Biomater. Sci.* **2013**, *1*, 1260.

[43] J. Linxweiler, C. Körbel, A. Müller, M. Hammer, C. Veith, R. M. Bohle, M. Stöckle, K. Junker, M. D. Menger, M. Saar, *Prostate* **2018**, *78*, 664.

[44] E. J. Ngen, B. Benham Azad, S. Boinapally, A. Lisok, M. Brummet, D. Jacob, M. G. Pomper, S. R. Banerjee, *Mol. Pharm.* **2019**, *16*, 2060.

[45] E. J. Ngen, Y. Chen, B. B. Azad, S. Boinapally, D. Jacob, A. Lisok, C. Shen, M. S. Hossain, J. Jin, Z. M. Bhujwalla, M. G. Pomper, S. R. Banerjee, *Nanotheranostics* **2021**, *5*, 182.

[46] C. A. Schneider, W. S. Rasband, K. W. Eliceiri, *Nat. Methods* **2012**, *9*, 671.

[47] P. R. Clark, W. Chua-Anusorn, T. G. Pierre, *Magn. Reson. Imaging* **2003**, *21*, 519.

[48] P. Storey, A. A. Thompson, C. L. Carqueville, J. C. Wood, R. A De Freitas, C. K. Rigsby, *J. Magn. Reson. Imaging* **2007**, *25*, 540.

[49] P. Spincemaille, J. Anderson, G. Wu, B. Yang, M. Fung, Ke Li, S. Li, I. Kovanlikaya, A. Gupta, D. Kelley, N. Benhamo, Yi Wang, *J. Neuroimaging* **2020**, *30*, 65.

[50] E. Amstad, M. Textor, E. Reimhult, *Nanoscale* **2011**, *3*, 2819.

[51] J. Y. Oh, H. S. Kim, L. Palanikumar, E. M. Go, B. Jana, S. Ah Park, Ho. Y Kim, K. Kim, J. K. Seo, S. K. Kwak, C. Kim, S. Kang, Ja-H Ryu, *Nat. Commun.* **2018**, *9*, 4548.

[52] E. Krepela, Z. Vanickova, P. Hrabal, M. Zubal, B. Chmielova, E. Balaziova, P. Vymola, I. Matrasova, P. Busek, A. Sedo, *Int. J. Mol. Sci.* **2021**, *22*, 1046.

[53] D. V. Tyulkina, V. V. Pleshkan, I. V. Alekseenko, M. R. Kopantseva, E. D. Sverdlov, *Dokl. Biochem. Biophys.* **2016**, *470*, 319.

[54] A. Ben Jemaa, S. Sallami, J. Céraline, R. Oueslati, *Cell Biol. Int.* **2013**, *37*, 464.

[55] W. Liu, Y. Zhu, L. Ye, Y. Zhu, Y. Wang, *Transl. Cancer Res.* **2021**, *10*, 3268.

[56] J. S. Wysock, H. Lepor, *Transl. Androl. Urol.* **2017**, *6*, 453.

[57] L. M. Ebert, W. Yu, T. Gargett, J. Toubia, P. M. Kollis, M. N. Tea, B. W. Ebert, C. Bardy, M. Van Den Hurk, C. S. Bonder, J. Manavis, K. S. Ensbey, M. Oksdath Mansilla, K. G. Scheer, S. L. Perrin, R. J. Ormsby, S. Poonnoose, B. Koszyca, S. M. Pitson, B. W. Day, G. A. Gomez, M. P. Brown, *Clin. Transl. Immunol.* **2020**, *9*, 1191.

[58] V. Cremasco, J. L. Astarita, A. L. Grauel, S. Keerthivasan, K. Macisaac, M. C. Woodruff, M. Wu, L. Spel, S. Santoro, Z. Amoozgar, T. Laszewski, S. C. Migoni, K. Knoblich, A. L. Fletcher, M. Lafleur, K. W. Wucherpfennig, E. Pure, G. Dranoff, M. C. Carroll, S. J. Turley, *Cancer Immunol. Res.* **2018**, *6*, 1472.

[59] L. Tao, G. Huang, H. Song, Y. Chen, L. Chen, *Oncol. Lett.* **2017**, *14*, 2611.

[60] H. Du, G. Che, *Oncol. Lett.* **2017**, *13*, 3.

[61] S. A. Koerber, K. Sprute, C. Kratochwil, E. Winter, M. F. Haefner, S. Katayama, I. Schlampp, K. Herfarth, K. Kopka, A. Afshar-Oromieh, S. Zschaebitz, T. Holland-Letz, P. L. Choyke, D. Jaeger, M. Hohenfellner, U. Haberkorn, J. Debus, F. L. Giesel, *Eur. J. Nucl. Med. Mol. Imaging* **2021**, *48*, 143.

[62] R. Mazzola, F. Cuccia, V. Figlia, M. Rigo, L. Nicosia, N. Giaj-Levra, F. Ricchetti, C. Vitale, B. Mantoan, G. Di Paola, A. De Simone, D. Gurrera, G. Sicignano, S. Naccarato, R. Ruggieri, F. Alongi, *Radiol. Med.* **2021**, *126*, 989.

[63] S. E. Serfling, P. E. Hartrampf, Y. Zhi, T. Higuchi, S. P. Rowe, L. Bundschuh, M. Essler, A. K. Buck, R. Alexander Bundschuh, R. A. Werner, *Clin. Nucl. Med.* **2022**, *47*, 512.

[64] F. De Felice, A. Piccioli, D. Musio, V. Tombolini, *OncoTargets Ther.* **2017**, *8*, 25691.

[65] E. G. Isik, D. Has-Simsek, O. Sanli, Y. Sanli, S. Kuyumcu, *Clin. Nucl. Med.* **2022**, *47*, 54.

[66] S. Vaz, B. Hadaschik, M. Gabriel, K. Herrmann, M. Eiber, D. Costa, *Eur. J. Nucl. Med. Mol. Imaging* **2020**, *47*, 9.

[67] R. Otazo, P. Lambin, J.-P. Pignol, M. E. Ladd, H.-P. Schlemmer, M. Baumann, H. Hricak, *Radiology* **2021**, *298*, 248.

[68] G. A. Sonn, R. E. Fan, P. Ghanouni, N. N. Wang, J. D. Brooks, A. M. Loening, B. L. Daniel, K. J. To'o, A. E. Thong, J. T. Leppert, *Eur. Urol. Focus* **2019**, *5*, 592.

[69] A. Priester, S. Natarajan, P. Khoshnoodi, D. J. Margolis, S. S. Raman, R. E. Reiter, J. Huang, W. Grundfest, L. S. Marks, *J. Urol.* **2017**, *197*, 320.

[70] S. J. Hectors, S. Semaan, C. Song, S. Lewis, G. K. Haines, A. Tewari, A. R. Rastinehad, B. Taouli, *Radiology* **2018**, *286*, 918.

[71] S. G. Nerella, P. Singh, T. Sanam, C. S. Digwal, *Front. Med.* **2022**, *9*, 812270.

[72] S. M. Cromer Berman, P. Walczak, J. W. M. Bulte, *Wiley Interdiscip. Rev.: Nanomed. Nanobiotechnol.* **2011**, *3*, 343.

[73] W. Hong, Q. He, S. Fan, M. Carl, H. Shao, J. Chen, E. Y. Chang, J. Du, *Magn. Reson. Med.* **2017**, *78*, 226.

[74] J. Niedermeyer, M. J. Scanlan, P. Garin-Chesa, C. Daiber, H. H. Fiebig, L. J. Old, W. J. Rettig, A. Schnapp, *Int. J. Cancer* **1997**, *71*, 383.

[75] J. Niedermeyer, M. Kriz, F. Hilberg, P. Garin-Chesa, U. Bamberger, M. C. Lenter, J. Park, B. Viertel, H. PüSchner, M. Mauz, W. J. Rettig, A. Schnapp, *Mol. Cell. Biol.* **2000**, *20*, 1089.

[76] W. N. Brennen, D. M. Rosen, H. Wang, J. T. Isaacs, S. R. Denmeade, *J. Natl. Cancer Inst.* **2012**, *104*, 1320.

[77] S. Sindhwani, A. M. Syed, J. Ngai, B. R. Kingston, L. Maiorino, J. Rothschild, P. Macmillan, Y. Zhang, N. U. Rajesh, T. Hoang, J. L. Y. Wu, S. Wilhelm, A. Zilman, S. Gadde, A. Sulaiman, B. Ouyang, Z. Lin, L. Wang, M. Egeblad, W. C. W. Chan, *Nat. Mater.* **2020**, *19*, 566.

[78] Md. A Subhan, S. S. K. Yalamarty, N. Filipczak, F. Parveen, V. P. Torchilin, *J. Pers. Med.* **2021**, *11*, 571.

[79] A. Hoffmann, B. Oborn, M. Moteabbed, S. Yan, T. Bortfeld, A. Knopf, H. Fuchs, D. Georg, J. Seco, M. F. Spadea, O. Jäkel, C. Kurz, K. Parodi, *Radiat. Oncol.* **2020**, *15*, 129.